



**HAL**  
open science

## O<sub>2</sub> and OH Night Airglow Emission Derived from GOMOS-Envisat Instrument

Christophe Bellisario, Philippe Keckhut, Laurent Blanot, Alain Hauchecorne,  
Pierre Simoneau

► **To cite this version:**

Christophe Bellisario, Philippe Keckhut, Laurent Blanot, Alain Hauchecorne, Pierre Simoneau. O<sub>2</sub> and OH Night Airglow Emission Derived from GOMOS-Envisat Instrument. *Journal of Atmospheric and Oceanic Technology*, 2014, 31 (6), pp.1301-1311. 10.1175/JTECH-D-13-00135.1 . hal-00968748

**HAL Id: hal-00968748**

**<https://hal.science/hal-00968748>**

Submitted on 22 Nov 2020

**HAL** is a multi-disciplinary open access archive for the deposit and dissemination of scientific research documents, whether they are published or not. The documents may come from teaching and research institutions in France or abroad, or from public or private research centers.

L'archive ouverte pluridisciplinaire **HAL**, est destinée au dépôt et à la diffusion de documents scientifiques de niveau recherche, publiés ou non, émanant des établissements d'enseignement et de recherche français ou étrangers, des laboratoires publics ou privés.

## O<sub>2</sub> and OH Night Airglow Emission Derived from GOMOS-*Envisat* Instrument

CHRISTOPHE BELLISARIO

*DOTA, ONERA, Palaiseau, France*

PHILIPPE KECKHUT

*LATMOS-IPSL, CNRS/INSU, UMR 8190, Université de Versailles Saint-Quentin-en-Yvelines, Guyancourt, France*

LAURENT BLANOT

*ACRI-ST, Sophia-Antipolis, France*

ALAIN HAUCHECORNE

*LATMOS-IPSL, CNRS/INSU, UMR 8190, Université de Versailles Saint-Quentin-en-Yvelines, Guyancourt, France*

PIERRE SIMONEAU

*DOTA, ONERA, Palaiseau, France*

(Manuscript received 21 June 2013, in final form 7 February 2014)

### ABSTRACT

Global Ozone Monitoring by Occultation of Stars (GOMOS) was an instrument dedicated to the study of atmospheric chemistry based on the principle of stellar occultation. The signals delivered by the IR spectrometer coupled with two CCD detectors, initially used for absorption measurements, were analyzed in order to observe the night airglow resulting from O<sub>2</sub> and OH emissions at 761.9 and 930 nm, respectively. The method to retrieve those emissions is described as well as the error analysis. The results of this first attempt are presented and discussed with respect to instrument characteristics, earth coverage, altitude resolution, and the ability of GOMOS data to contribute to night airglow investigations. Mean limb intensities are equal to 28.9 and 7.7 MR for O<sub>2</sub> at 760 nm and OH at 930 nm, respectively. Individual O<sub>2</sub> emissions are retrieved with an accuracy better than 15%, while the OH emission, which provides smaller intensities, is retrieved with an accuracy of 10% for the monthly average.

### 1. Introduction

In the near-infrared (IR) region, the mesospheric nightglow takes its sources mainly in the emission lines photochemically produced by OH radicals, O<sub>2</sub> atmospheric bands, and atomic oxygen. This effect was first reported by Meinel (1950) and received a lot of interest in order to better understand the physics of the upper mesosphere. The IR emission band is wide and takes place from 700 nm to a few microns. Airglow observation can be useful to better understand atmospheric

phenomena that remain in question, such as the solar forcing on climate through the NO<sub>x</sub> chemistry (Solomon et al. 1999), the role of the gravity waves (Hines 1960; Alexander et al. 2010) and atmospheric tides on the vertical atmospheric coupling, the detection of the cooling expected in the upper mesosphere due to the increase of greenhouse gases (Beig et al. 2003), and the occurrence of noctilucent clouds (Gadsden 1998; Pérot et al. 2010).

Since the beginning of last century, the mesospheric nightglow emissions have been studied, mainly with ground-based observations (McLennan and McLeod 1927; Slipher 1929), then with rockets (Heppner and Meredith 1958), and finally with satellites at the beginning of the 1970s. The *International Satellites for Ionospheric Studies II (ISIS-II; Shepherd et al. 1973)*, the *Orbiting Geophysical Observatory 6 (OGO 6; Donahue*

---

*Corresponding author address:* Christophe Bellisario, DOTA, ONERA, Chemin de la Hunière, BP 80100, 91123 Palaiseau CEDEX, France.  
E-mail: christophe.bellisario@onera.fr

et al. 1974) and the *Atmospheric Explorer* (AE; AE-C, AE-D, and AE-E) (Torr et al. 1977) were the first satellite programs to provide airglow data, allowing one to understand the nightglow variations. While the OH band at  $1.6\ \mu\text{m}$  is clearly observed with ground-based instruments, the brightest band at  $4\ \mu\text{m}$  is absorbed in the lower atmosphere, thus requiring the satellite observations. In addition, observations of other components like alkali metals (Delannoy and Weill 1958) were performed simultaneously, providing useful information about the physical processes occurring at these altitudes (Meriwether 1989). Nowadays, these measurements are still valuable for the validation of numerical models describing the molecular and ionospheric chemistry, wave forcing from below, from above (solar particle precipitations, meteorite showers, etc.), and coupling mechanisms (dynamic).

On board the European Space Agency's (ESA) space platform the *Environmental Satellite* (*Envisat*), the Global Ozone Monitoring by Occultation of Stars (GOMOS) instrument, operational from March 2002 to April 2012, was dedicated to the study of the earth's atmosphere (Bertaux et al. 2004). Its sun-synchronous orbit implied each location to be seen at almost the same local time. It is an essential characteristic, since it allows long-term trends not to be disturbed by tides and by the diurnal photolysis mechanism. The method of star occultation allowed for deriving limb vertical profiles of constituents like ozone with a good vertical resolution (about 2 km). The GOMOS instrument provided atmospheric spectrum from 248 to 954 nm. The emissions associated with species like  $\text{O}_2$  and OH could then be observed. Such long continuous and global observations are highly valuable for investigating the atmospheric variability on different time scales from gravity waves to interannual changes. Other instruments allow airglow observations from space. The Sounding of the Atmosphere using Broadband Emission Radiometry (SABER) infrared radiometer is designed for energetics and temperature measurements (Mlynczak 1997), and it looks over the OH emission spectral window at 1.6 and  $2\ \mu\text{m}$ . Two decades ago, the Wind Imaging Interferometer (WINDII), dedicated to wind profile measurements (Melo et al. 2000), observed the OH (8–3) band at 730 nm and also the  $\text{O}_2$  (0–0) atmospheric band at 760 nm (among other species). The Scanning Imaging Absorption Spectrometer for Atmospheric Cartography (SCIAMACHY) was focused on limb emission data (Kaufmann et al. 2008) with OH observations of the (9–6) and (3–1) bands. GOMOS was the first satellite instrument able to measure the OH (8–4) band and to continue measurements on the  $\text{O}_2$  (0–0) bands, as WINDII stopped in 2004.

Although the GOMOS instrument was not designed for airglow measurements, it is valuable to describe signal averaging strategies, to mitigate uncertainties, and to report about the final accuracy. In this paper, the method to analyze the GOMOS spectrum in the near-infrared (NIR) region in order to investigate the  $\text{O}_2$  and OH emissions is presented. The concern is to describe the measurement conditions that may introduce noises. We extract the real signal corresponding to the airglow and address the averaging issues. We aim to provide the best compromise between quality and quantity of original data.

In section 2, we describe the instrument, its purpose, and we provide information about the two-band spectrometer used in this study. In section 3, the impact of the measurements' conditions on the retrieval is analyzed with emphasis on the data selection. In section 4, we provide a detailed description of the processing chain that we developed in the frame of this study, including conversion of the raw spectra into physical units, stray light (defined later) removal, and computation of the nightglow intensity and its associated error bars. Finally, in section 5, the first results of  $\text{O}_2$  and OH nightglows are presented and discussed.

## 2. GOMOS instrument and data overview

GOMOS is on board the *Envisat* space platform with nine other instruments partially dedicated to the study of atmospheric chemistry (Bertaux et al. 2010). The sun-synchronous satellite is located at an average altitude of 800 km, with an orbit inclination of  $98.55^\circ$ . It especially allows for building a 3D distribution of ozone in the middle atmosphere with high accuracy in altitude thanks to the technique of occultation of stars mainly in the stratosphere and also in the mesosphere, where the second ozone maximum was accurately observed (Evans and Llewellyn 1972). GOMOS is looking backward, recording the spectrum of a star to determine absorption through the Beer–Lambert law with a  $30\text{ cm} \times 15\text{ cm}$  (1.05-m focal length) telescope. As the *Envisat* platform is moving along its orbit, the light spectrum of a given star is continuously recorded, with a line of sight (LOS) crossing atmospheric air masses located at lower altitudes (Fig. 1). The ratio between the spectrum observed outside the atmosphere and the spectrum through the atmosphere gives a transmission spectrum where the absorption bands of a given molecule can be identified. This absorption signature is related to the concentration integrated along the LOS. The integration time is 0.5 s and the velocity of the tangent point is  $3.4\text{ km s}^{-1}$ , so that the vertical sampling resolution is 1.7 km at most. There are occultations called tangent or oblique, where the

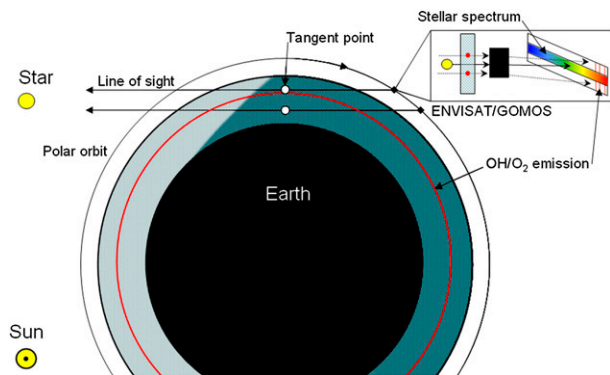


FIG. 1. Principle of O<sub>2</sub> and OH observation. While the *Envisat* platform is moving along its orbit, the altitude of the tangent point decreases and the atmospheric absorption of the star spectrum varies for ozone measurements recorded on the central CCD band. The nightglow emission layer is indicated in red. When the LOS is crossing the altitude of airglow emission, the GOMOS upper and lower CCD bands allow limb view observations of the OH and O<sub>2</sub> emissions.

descent speed of the tangent point is much smaller. As a result the vertical sampling is better (one measurement every 0.15 km), but the resolution is limited to 600 m by the size of the detector. In comparison, the vertical resolution using other instruments (SABER or WINDII) reporting airglow observations is 2 km for the final product.

GOMOS is composed of two spectrometers (A and B), each using two charge-coupled devices (CCDs; 1 and 2). Therefore, four spectral intervals are considered—A1, from 248.1 to 389.18 nm (UV); A2, from 389.52 to 690.49 nm [visible (VIS)]; B1, from 755.12 to 774.59 nm; and B2, from 925.97 to 954.42 nm (for NIR). Each CCD uses three stripes [or bands as defined in Bertaux et al. (2010); see Fig. 1], defined as follows:

- The central band is collecting the star target flux.
- The upper band and the lower band (called background bands) are looking above and below the star, respectively. When they observe a dark sky area at night, the results are used in the processing chain for the dark charge correction.

In our study, B1 and B2 background band spectra (both upper and lower) are used in order to look for the O<sub>2</sub> (0–0) atmospheric band and OH (8–4) emission bands, respectively (see Fig. 2 with the given OH lines). In this case, OH and O<sub>2</sub> emissions can be extracted from the upper and lower band signals, while in the central band, the star spectrum masks such emissions. The spectral coverage of each pixel corresponds to 0.047 nm for B1 and 0.056 nm for B2. The slit of the spectrometer has a finite width of 10 pixels and the spectral resolution, due to the instrumental spectral point spread function (PSF), is 0.13 nm at full width at half maximum (FWHM). The pixel size is 20 μm × 27 μm and seven lines are used for each band.

GOMOS observed continuously star occultations from 2002 to April 2012. While it provides a very good time coverage compared with solar occultation (Bertaux et al. 2010), it also involves complex measurements. Indeed, each observation is performed with a very different signal-to-noise ratio, since star magnitudes are all different and background illumination can be different too. GOMOS measurements also suffer from a dark charge (DC) increase (Keckhut et al. 2010). In the present study, we have used the fifth version of the data processing. The residual signal of the CCD, the dark charge, corresponds to electrons generated in one pixel in the absence of incoming light. The DC correction is handled in the operational GOMOS processing chain: the DC estimate is made by pointing the GOMOS telescope

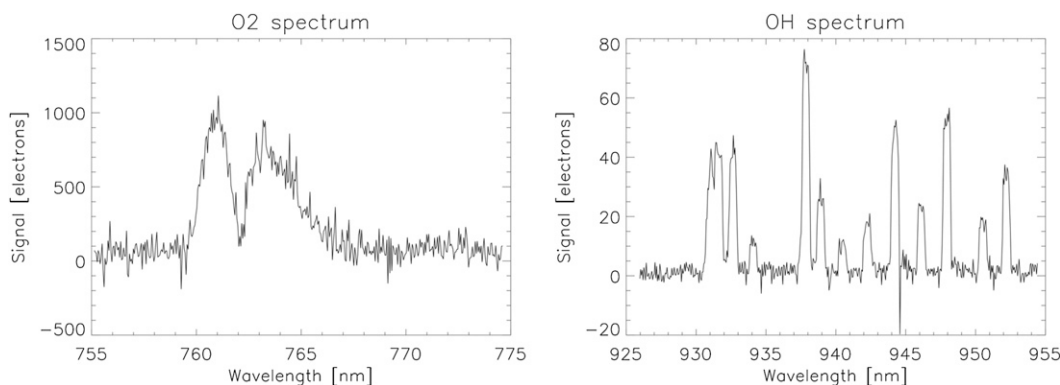


FIG. 2. (left) O<sub>2</sub> and (right) OH spectra in electrons. The O<sub>2</sub> spectrum was taken 1 Jan 2014 at 58° latitude and –57° longitude. The OH spectrum is averaged over the month of September 2002, over latitudes –15° and –10°, for all longitudes. On the OH spectrum, the R branch between 930 and 935 nm, the Q branch between 937 and 941 nm, and the P branch between 942 and 954 nm are visible.

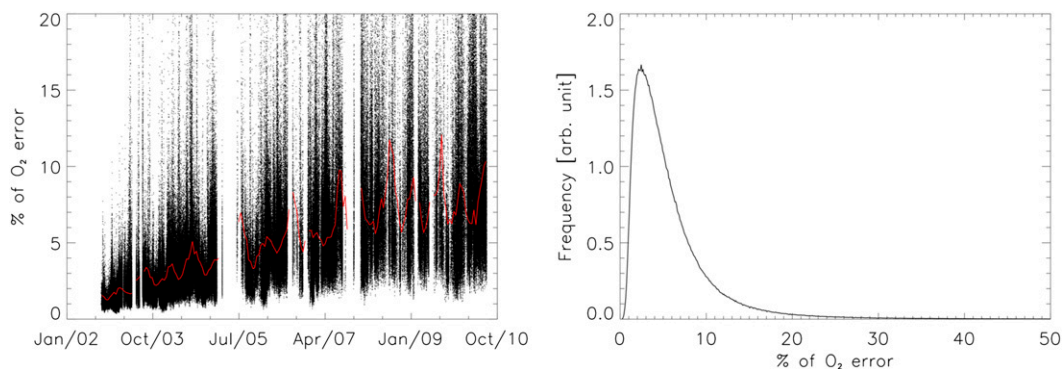


FIG. 3. (left) Evolution (%) of the error bars on the computed  $O_2$  nightglow during the years of GOMOS data. The positive linear trend appears to take its origin from the increase of the DC. (right) Distribution of the error with most of the values below 15%.

at night toward a dark sky area (DSA), that is, a portion of the sky where there is no star in the field of view. This measurement is planned for each orbit. A quasi-linear increase of the CCD DC through the time of the mission has been observed as represented in Fig. 3 (left). It is partially caused by the increase of the overall temperature of the instrument (degradation of external insulation) and the continuous increase of the CCDs' temperature, which are not cooled by design. The main cause of DC increase and detection limitation is the appearance of hot pixels [also called random telegraphic signal (RTS)]. These pixels exhibit erratic behaviors: a hot pixel is a pixel that can suddenly deliver a lot of electrons during a short amount of time (seconds or minutes, sometimes more) and then come back to its initial state. Cosmic particles, especially during transits through the South Atlantic anomaly, are mainly responsible for the increasing number of hot pixels. This massive increase of the number of hot pixels through the mission results in an increase of the average DC.

In 2005, some malfunctions of the mirror mechanism led to an interruption of the measurements for several months. Following this interruption, the measurements restarted with a restricted azimuth range leading to a decrease of the earth's coverage. The average number of occultations per day decreased from about 400 to 250–300.

### 3. Measurement conditions and data selection

#### a. Illumination conditions

The position of the satellite above the earth and the limb illumination are also a source of stray light according to the conditions of illumination of the portion of the scene directly observed by GOMOS. It is also caused by light coming from other atmospheric regions. In the data files provided by the European Space Agency (ESA),

a specific flag condition called product confidence data (PCD) describes these illumination conditions. It depends mainly on the sun's position with respect to the satellite and the illumination conditions of the tangent point. Three types of illumination conditions are identified, while the satellite can be also directly illuminated, providing more stray light.

Condition 0 corresponds to full dark, where the tangent point and the satellite are in full dark. Condition 1 is the opposite, where both the tangent point and the satellite are in full-day conditions. Condition 2 refers to twilight, meaning that the satellite is in full dark and the tangent point illumination is in twilight [solar zenith angle (SZA) < 110°]. Condition 3 corresponds to "stray light," where the tangent point is in full dark and the satellite might be illuminated (SZA < 120°). To finish, condition 4 is the combination of conditions 2 and 3. All illumination conditions are summarized in Table 1.

According to the conditions described in section 3a, the data for illumination conditions 1 and 4 are never and hardly selected in our study, respectively, whereas conditions 2 and 3 are sometimes selected. PCD conditions 2–4 are found for observations located at high latitudes (south and north), which implies that the measurements' conditions were less favorable in these regions. The restriction of the data to only full-dark conditions will remove parts of the GOMOS coverage but will provide the lowest noise level and the most accurate measurements.

#### b. Other causes of stray light

Two major sources of light contamination that contribute to recorded signals were considered:

- the aurora emission lights
- the external stray light

Both phenomena are described hereafter.

TABLE 1. Illumination conditions, as a function of the tangent point and satellite illumination. Full-day condition is defined as SZA at tangent point  $<97^\circ$  for at least one measurement with altitude at tangent point  $<50$  km, and full dark is none of the other conditions.

Condition No.	Illumination condition name	Tangent point illumination	Satellite illumination
0	Full_dark	Full dark	Full dark
1	Bright_limb	Full day	Full day
2	Twilight	Twilight (SZA $< 110^\circ$ )	Full dark
3	Stray light	Full dark	SZA $< 120^\circ$
4	Twilight + stray light	Twilight (SZA $< 110^\circ$ )	SZA $< 120^\circ$

### 1) AURORA EMISSION LIGHTS

GOMOS measurements may be affected by auroral emission lights. This happens generally for observations located near the poles. The spectral signature of the auroral light has several emission lines located in the UV, visible, and near IR. The most intense line is the green line, located at 557.7 nm in spectrometer A2. The line is due to the emission of atomic oxygen. An aurora light detection algorithm has been built, based on the presence of the green line. If the green line is detected above 80 km, then an “aurora flag” is raised for the current GOMOS observations. It is important to flag observations contaminated by an aurora. The top panel in Fig. 4 represents one aurora case, where the atomic green line is saturated as well as the O<sub>2</sub> emission signal on the spectrometer

B1 (SPB1). As a comparison, the bottom panel in Fig. 4 shows the upper-band signal with no aurora.

### 2) EXTERNAL STRAY LIGHT

The term *external stray light* is used to qualify the light originating from outside the line of sight of the instrument. In other terms, it is the light that is not supposed to reach the instrument detectors. There are two main sources of external stray light: one is the possible reflection of solar light on *Envisat* components or on GOMOS optical system components. The other source is the scattering of the solar light due to molecules or particles that are outside the field of view but are illuminating a part of GOMOS—for instance, the front plane mirror, which scatters again in all directions,

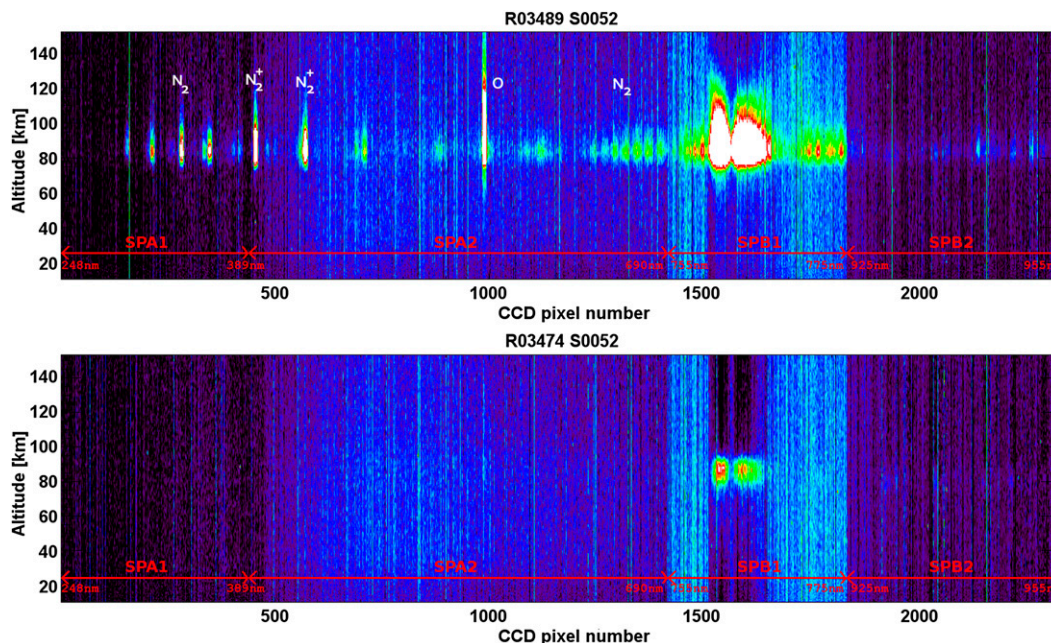


FIG. 4. Upper-band signal for a GOMOS observation (top) with a strong aurora and (bottom) without. The x axis is the spectral dimension. The unit is the pixel number, with each pixel number being associated with a wavelength. The legend shows the separation between the four CCD spectrometers: SPA1, SPA2, SPB1, and SPB2. (top) Several aurora emission lines are visible near 90 km. Among them, the “green line” at 557 nm (near pixel 1000) is used for the aurora detection algorithm. The O<sub>2</sub> emission signal amplitude at 760 nm (between pixels 1500 and 1600) is strongly increased by the presence of the aurora.

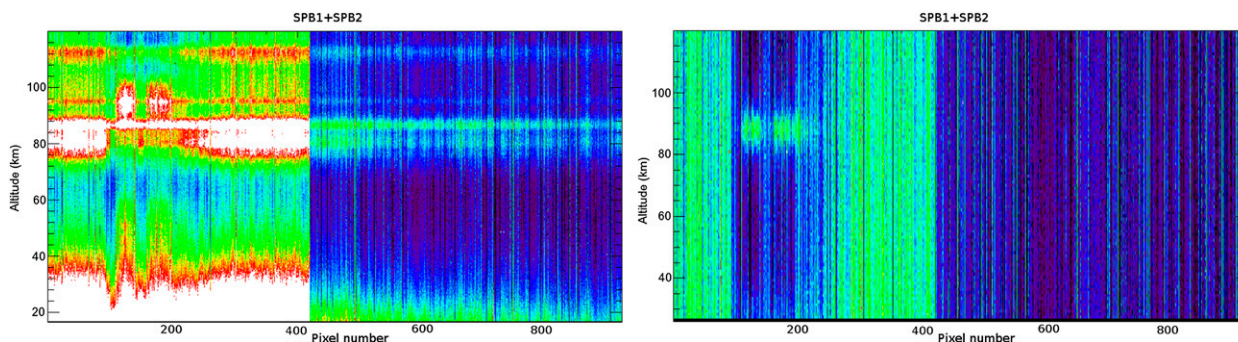


FIG. 5. Two examples of GOMOS upper-band observation with stray-light contamination. Only SPB1 (pixels 0–420) and SPB2 (pixels 421–920) are represented. (left) A case where stray light varies a lot with the altitude (see pixels 0–200 and 220–420). (right) A case where the stray light does not vary with altitude. For this case, the stray light can be corrected: we estimate it by averaging the spectra above 110 km (no airglow at these altitudes). We then subtract this averaged spectrum from the spectra at all other altitudes. Therefore, in our selection method, the (left) case is flagged (discarded), whereas the (right) case is not. The  $O_2$  emission is visible in both cases in SPB1 between pixels 100 and 200 near 90 km.

including the nominal field of view. It has been shown that this contribution is probably linked to the variation of albedo between the position of the tangent point and the position of the satellite, mainly due to the presence of very reflective tropospheric clouds. The presence of stray light is correlated with the SZA at the satellite position:

- For illumination conditions 0 and 2, SZA corresponds to large values and *Envisat* is in the dark. Thus, in this case, the data cannot be contaminated by any stray-light signal.
- For illumination conditions 1, 3, and 4, SZA has smaller values and *Envisat* is illuminated by the sun, leading to possible stray-light contamination.

In the nominal processing of star occultation, the sky background and the stray light are removed by subtracting the upper- and lower-band signals from the central band containing the star spectrum. As a result, there is no dedicated stray-light correction of upper and lower bands in the GOMOS ESA operational processing and thus the presence of stray light in the background band can severely bias our study. In the frame of this study, a GOMOS stray-light flag algorithm has been specifically developed. We check for the presence of the stray light signal in the spectrometer B1 (SPB1). The stray-light flag is raised if at least one of the two following items is verified:

- The level of the stray-light signal exceeds a threshold level.
- The variation of the stray-light signal intensity between the first measurement (highest altitude) and the measurement corresponding to 80-km altitude exceeds a certain threshold (slope). Figure 5 (left) gives an example of stray-light signal showing a strong change of intensity with altitudes.

If none of these points is verified, then we can consider that either there is no stray-light signal or the stray-light signal is stable enough so that it can be efficiently removed by the subtraction of the high-altitude spectrum (mean spectrum  $> 110$  km). Thus, the observation is not flagged, as we can see in Fig. 5 (right). If a flag is raised in SPB1, then we raise it also for spectrometer B2 (SPB2). Indeed, the stray-light signal presence in SPB1 and its fluctuation with altitude are generally similar in SPB2 (with a much smaller intensity in SPB2, but it may still bias the OH emission line retrieval, as these lines are very faint).

## 4. Retrieval method description

### a. Noise contamination and removal

One of the main problems with instrumental data is the estimate of noise to be subtracted from the raw signal. The different sources of noise that must be considered in the frame of our study are stray light, stellar leakage, and residual dark charge. More information about these noises is given below.

#### 1) STRAY LIGHT

The stray-light origin and signature are explained in section 3b(2).

#### 2) RESIDUAL DC

The GOMOS CCDs' dark charge signal is corrected in the GOMOS level 1b processing chain. However, this correction is not a perfect one: indeed, the temperature of the CCD that is used in the DC correction algorithm is measured with a discretization step of  $0.4^\circ$ . This can lead to an error in the dark charge estimate of up to 6%.

#### 3) STELLAR LEAKAGE

As the star is a point source, its image on the CCD in a perfect instrument should be spatially focused in

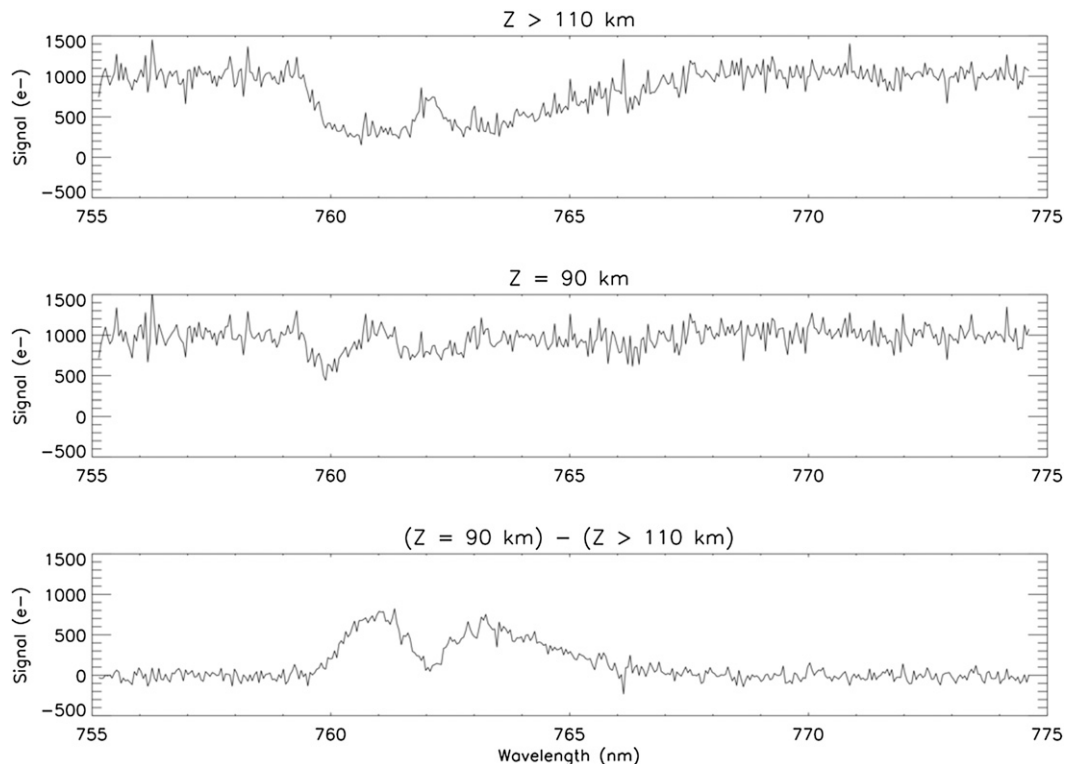


FIG. 6. Process of noise removal (here with an  $O_2$  spectrum). (top) The first spectrum, observed at altitudes higher than 110 km, is subtracted from (middle) the spectrum observed at 90 km. (bottom) The result is a spectrum corrected from stray-light contamination. The (top) contains the strong  $O_2$  absorption A band. Indeed, this signal is due to solar light scattered by the ground, clouds, or lower atmosphere. It is not solar light scattered by the spacecraft, which would contain no  $O_2$  signature.

the central band. However, the spatial PSF of GOMOS spreads the projection of the star. As a consequence, some signals reach the upper and lower bands. This contamination is called stellar leakage. The amount of signal received in the background bands is about 1% of the signal in the central band.

We have developed an algorithm in order to correct these three sources of contamination. This algorithm is based on the fact that these three sources do not vary with the altitude. Indeed,

- the dark charge is constant for a time scale of one observation (about 1 min);
- the star leakage is proportional to the star signal in the central band, which is constant for the altitudes considered in our study (no absorption above 80 km in SPB); and
- our stray-light flagging routine has discarded all the data with stray light varying strongly with altitude.

A high-altitude spectrum is computed by averaging all spectra above 110 km (Fig. 6, top). This spectrum is an estimator of the cumulated signal of the three sources of contamination. This high-altitude spectrum is then

removed from all the spectra between 80 and 100 km, as illustrated in Fig. 6. This provides contamination-corrected spectra. The  $O_2$  spectrum can be identified more clearly after noise removal (Fig. 6, bottom).

Despite the removal of the high-altitude spectrum, there may be a small residual contamination signal in the case of the observations with a stray-light signal slightly varying with altitude that has not been flagged by the stray-light detection routine. When computing the airglow intensity signal by integrating the signal over wavelengths, this residual noise, called here “the base,” is calculated by averaging the signal outside the emission line. This residual noise signal is then subtracted to estimate the correct airglow signal (Fig. 6). The detailed calculations of the error estimates are described in the next section.

#### *b. Computation of the nightglow intensity and error estimate*

To compute the nightglow intensity at a given altitude  $z$ , several steps are required. The GOMOS limb products are provided in the unit of electrons  $0.5 \text{ s}^{-1} \text{ pixel}^{-1}$ . A radiometric conversion factor is used to obtain a physical unit: photons  $\text{cm}^2 \text{ s}^{-1} \text{ nm}^{-1} \text{ sr}^{-1}$ . The number

of electrons  $N(e)$  created per pixel during  $dt$  may be written as

$$N(e) = I(\lambda) d\omega S_{\text{eff}}(\lambda) d\lambda dt, \quad (1)$$

where

$I(\lambda)$  is the brightness of the emission in photons  $\text{cm}^2 \text{s}^{-1} \text{sr}^{-1} \text{nm}^{-1}$ ;

$d\omega$  is the solid angle subtended by the instantaneous FOV, defined by the width of the slit in pixels (10 pixels), the height of the CCD band (7 pixels), the size of one pixel ( $20 \mu\text{m} \times 27 \mu\text{m}$ ), and the focal length of the telescope ( $f = 1.05 \text{ m}$ ):

$$d\omega = \frac{10 \times 7 \times 20 \times 10^{-6} \times 27 \times 10^{-6}}{1.05^2} = 3.42 \text{ sr}; \quad (2)$$

$S_{\text{eff}}(\lambda)$  is the efficient area of GOMOS, with an average value of 1.17 and 0.63 electrons photons $^{-1}$  ( $\text{s nm cm}^2$ ) $^{-1}$  for SPB1 and SPB2, respectively.

From the spectrum  $S^z \pm \sigma^z$  in  $0.5 \text{ s}^{-1} \text{ pixel}^{-1}$ , a high-altitude averaged spectrum  $S^h \pm \sigma^h$  is subtracted, where  $S^{z,h}$  is the spectrum at altitude  $z$  or high altitude  $h$ , and  $\sigma$  is the uncertainty. This allows the removal at once of several noise sources, as explained in the previous section, where

$$S_{0i} = S_i^z - S_i^h. \quad (3)$$

The uncertainty for each pixel  $i$  is consequently

$$\sigma_i = \sqrt{(\sigma_i^z)^2 + (\sigma_i^h)^2}, \quad (4)$$

with  $\sigma_i^z$  being the uncertainty associated with the pixel  $i$  at altitude  $z$  and  $\sigma_i^h$  for high altitudes.

Then we proceed to a sum over the wavelengths domain belonging to the signature ( $R_0 \pm \sigma_{R0}$ ) and an average for the basis ( $b \pm \sigma_b$ ):

$$R_0 = \sum_{\lambda_R} S_0 \quad \text{and} \quad b = \overline{S_0}_{\lambda b}, \quad (5)$$

$$\sigma_{R0} = \sqrt{\sum_{\lambda R} (\sigma_i)^2} = \sqrt{\sum_{\lambda R} [(\sigma_i^z)^2 + (\sigma_i^h)^2]}, \quad \text{and} \quad (6)$$

$$\sigma_b = \frac{\sqrt{\sum_{\lambda b} (\sigma_i)^2}}{n_b} = \frac{\sqrt{\sum_{\lambda b} [(\sigma_i^z)^2 + (\sigma_i^h)^2]}}{n_b}. \quad (7)$$

Finally, a possible remaining offset is removed. For achieving this estimate, the average value corresponding to the pixels around the signal (the bases) is computed

and subtracted from the signal (times  $n_R$ , the number of signal pixels due to the sum over the signal). Then, we obtain the final nightglow using

$$R = R_0 - n_R b \quad (8)$$

with its associated uncertainty estimate defined as

$$\begin{aligned} \sigma_R &= \sqrt{\sigma_{R0}^2 + (n_R \sigma_b)^2} \\ &= \sqrt{\sum_{\lambda R} [(\sigma_i^z)^2 + (\sigma_i^h)^2] + \frac{n_R^2}{n_b^2} \sum_{\lambda b} [(\sigma_i^z)^2 + (\sigma_i^h)^2]}. \end{aligned} \quad (9)$$

The conversion in Rayleigh unit is performed with the knowledge that 1 Rayleigh equals  $(10^6/4\pi)$  photons  $\text{cm}^2 \text{s}^{-1} \text{sr}^{-1}$ .

## 5. Preliminary results

The signal analysis of the  $\text{O}_2$  and  $\text{OH}$  airglow derived in the previous sections leads to a significant amount of data (about 5.4 million points of data usable in case of  $\text{O}_2$  airglow, with an average of 14 vertical points). The spatial and temporal coverage is large, from 2002 to 2010, with daily or monthly data for  $\text{O}_2$  and  $\text{OH}$  airglow over all longitudes and most of the latitudes, respectively. Indeed, 77% of available nights of measurements are used over 75% of the latitudes. For the monthly average, around 38% of the latitudes are considered.

Dealing with both  $\text{O}_2$  and  $\text{OH}$  spectra, a comparison between upper and lower bands has been made and a strong correlation is observed, as expected. Indeed, upper and lower bands are recorded at the same time and are thus supposed to measure the same signal under similar illumination conditions. Then, the global coverage is not homogeneous: as the PCD illumination conditions reduce the number of daytime observations, high latitudes during summer solar conditions may not be selected. To finish, the dataset reveals a decrease of valid observations at the highest latitudes in the summer hemisphere. For the Southern Hemisphere, there are no data below  $60^\circ\text{S}$  around January and similarly, there are no data above  $60^\circ\text{N}$  during summer in the Northern Hemisphere.

The local time is an important factor, as strong nocturnal variations can occur. Using GOMOS data, we observe that for the Northern Hemisphere, most of the observations are obtained before midnight, whereas in the Southern Hemisphere, observations are split around midnight. Variations of the nightglow in regard to the local time have already been studied by several teams (Yee et al. 1997; Abreu and Yee 1989). They show that a gradual decrease of  $\text{OH}$  emission (at  $732 \text{ nm}$ ) from

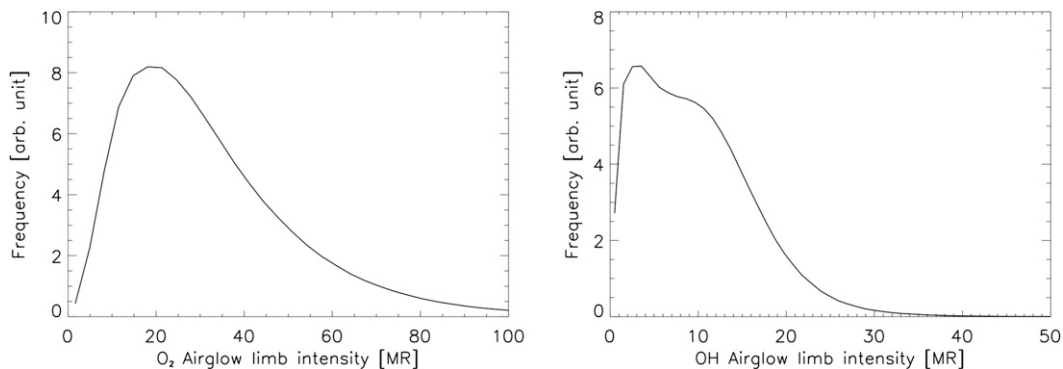


FIG. 7. Distributions of the airglow limb intensity—(left)  $O_2$  and (right)  $OH$ . The mean values of the airglow are 28.9 and 7.7 MR, respectively.

sunset to sunrise is observed at solstice. Thus, small effects are expected for the Northern Hemisphere, while there might be an underestimate of 20% of the nightglow in the Southern Hemisphere.

The observed airglow is a limb view airglow, which means that the whole line of sight contributes to the values presented below. The modified onion peeling method, the Abel inversion method, and the Tikhonov regularization (Sofieva et al. 2004) could be applied in order to perform comparisons with existing vertical profiles of local emissivities. It has not been derived using this method, as the signal-to-noise ratio of the individual spectra is low. For this reason, spectra have been averaged vertically and with time to access the geophysical variability. A vertical variability of the  $OH$  layer is expected on time scales shorter than a month and then it cannot easily be derived from these measurements.

The  $O_2$  airglow at high altitude is strong enough to be observed without averaging data. It takes values up to 100 MR. The error varies from 1% to 20%, as seen in Fig. 3 (right). The reason of the increase has already been explained in section 2. Figure 7 (left) shows the distribution of the  $O_2$  airglow. The average is around 28 MR and the distribution is positively skewed. For  $O_2$ , the optimal altitude corresponding to the maximum of nightglow takes place on average at 90 km (Fig. 8, left). However, we observe an altitude decrease of the peak close to the equator. In the region between  $15^\circ S$  and  $15^\circ N$ , the  $O_2$  emission is getting weaker, broader, and closer to the ground by a few kilometers (87–88 km) in comparison to other latitudes. In these latitudes, the variation in the airglow intensity between 90 km and the local maximum does not exceed 10%. Everywhere else, the maximum of intensity is included in a vertical domain of 2–3 km around 90 km.

Concerning the processing of  $OH$  emissions, the weakness of the signals has implied averaging the data. Bins of 1 month in time,  $5^\circ$  in latitude, and all longitudes

have been used in order to average the data. All illumination conditions have been kept. The  $OH$  nightglow takes values up to 30 MR, and it behaves differently among the latitudes, the average being observed around 7.7 MR. The altitude of the  $OH$  airglow maximum is observed at 85 km. Similar profiles has been found with SABER/the Thermosphere–Ionosphere–Mesosphere Energetics Dynamics (TIMED) satellite (Russell et al. 1999), or with ground-based observations (Suzuki et al. 2010). The peak height at the equator is also lower than those at other latitudes, which is consistent with the SABER/TIMED observations (with other  $OH$  bands; Gao et al. 2010). The average of the estimated error of the nightglow is around 12%. However, all illumination conditions are exploited, which may result in small deviations at high latitudes. Without averaging the data, the mean value of the limb intensity is slightly different (7.4 MR) but the error is larger (around 30%).

## 6. Conclusions and discussion

We have described in this study a way to use GOMOS data, initially planned for absorbing atmospheric constituents like ozone, in order to derive  $O_2$  and  $OH$  limb nightglow.

A data selection process has been developed using the raw data of the detectors dedicated for background noise estimates. Reliable observations have been selected through the use of the illumination condition and quality criteria, such as stray-light flag, aurora flag, and statistical tests.

Then, data were converted into physical units suitable for the estimate of the limb nightglow. The noise removal and the error estimate were explained as well as the process of selection of the specific wavelengths of the signal, with the use of the signal-to-noise optimization for  $O_2$ .

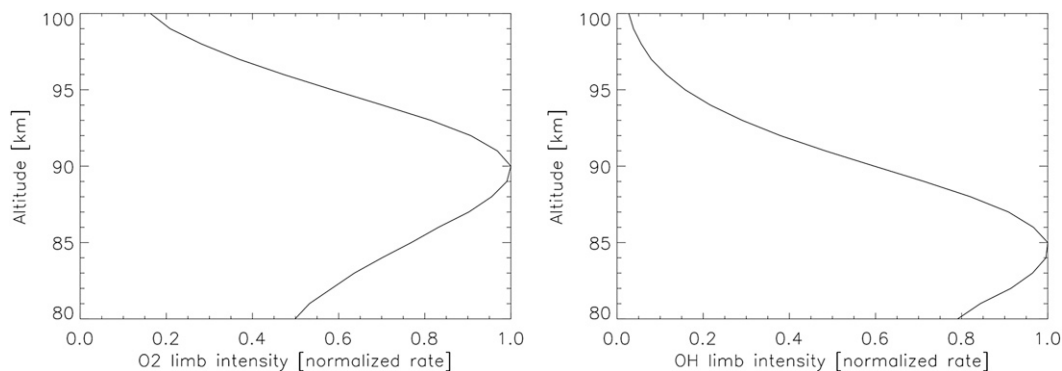


FIG. 8. Limb profiles of the (left) O<sub>2</sub> and (right) OH nightglows over all GOMOS data selected. The maximum intensity appears at 90 and 85 km, respectively.

Finally, preliminary climatological results were presented. The O<sub>2</sub> nightglow at 760 nm has a limb intensity around 30 MR at 90 km, with an associated error below 15%. The average intensity over a year for all latitudes and longitudes is 28.9 MR. For OH at 930 nm, the nightglow is fainter with an average of 7.7 MR at 85 km with a slightly smaller error (<10%).

We have also highlighted some considerations that have to be taken into account for the climatology of the nightglow. The local time of measurements may interfere with the nightglow intensity, as we do not separate observations according to solar local time, especially in the OH case.

Furthermore, the illumination conditions change partly with the latitude and impact the geographical sampling. With the criteria selected here, a compromise has been chosen between data coverage and high-quality data with the choice of PCD. It leads to a selection of 53.4% and 80% of all the GOMOS night data for the O<sub>2</sub> and OH nightglow investigations, respectively.

This study describing the methodology for airglow retrieval shows that GOMOS can be used to derive accurate airglow limb view emissions. In a follow-on study, this airglow database will be compared with other datasets and will be used for studying the variability of both emissions related to dynamical and external forcings. Climatology and interannual variability can be also investigated, since GOMOS measurements cover a decade. Such data are also valuable to validate chemistry-climate numerical models while the altitude range of these numerical models increases, including the mesopause region.

*Acknowledgments.* This work was supported by the Atmospheric Dynamics Research Infrastructure in Europe (ARISE), and the Direction Générale de l'Armement (DGA). The authors thank Jean-Loup Bertaux for his

useful comments. The GOMOS data were provided by ESA.

#### REFERENCES

- Abreu, V., and J. H. Yee, 1989: Diurnal and seasonal variation of the nighttime OH (8-3) emission at low latitudes. *J. Geophys. Res.*, **94**, 11 949–11 957, doi:10.1029/JA094iA09p11949.
- Alexander, M. J., and Coauthors, 2010: Recent developments on gravity-wave effects in climate models and the global distribution of gravity-wave momentum flux from observations and models. *Quart. J. Roy. Meteor. Soc.*, **136**, 1103–1124, doi:10.1002/qj.637.
- Beig, G., and Coauthors, 2003: Review of mesospheric temperature trends. *Rev. Geophys.*, **41**, 1015, doi:10.1029/2002RG000121.
- Bertaux, J.-L., and Coauthors, 2004: First results on GOMOS/ENVISAT. *Adv. Space Res.*, **33**, 1029–1035, doi:10.1016/j.asr.2003.09.037.
- , and Coauthors, 2010: Global ozone monitoring by occultation of stars: An overview of GOMOS measurements on ENVISAT. *Atmos. Chem. Phys.*, **10**, 12 091–12 148, doi:10.5194/acp-10-12091-2010.
- Delannoy, J., and G. Weill, 1958: Observation d'une nouvelle raie d'émission crépusculaire atmosphérique. *C. R. Acad. Sci.*, **247**, 806–807.
- Donahue, T. M., B. Guenther, and R. J. Thomas, 1974: Spatial and temporal behavior of atomic oxygen determined by Ogo 6 airglow observations. *J. Geophys. Res.*, **79**, 1959–1964, doi:10.1029/JA079i013p01959.
- Evans, W. F. J., and E. J. Llewellyn, 1972: Measurements of mesospheric ozone from observations of the 1.27- $\mu$  band. *Radio Sci.*, **7**, 45–50, doi:10.1029/RS007i001p00045.
- Gadsden, M., 1998: The north-west Europe data on noctilucent clouds: A survey. *J. Atmos. Sol. Terr. Phys.*, **60**, 1163–1174, doi:10.1016/S1364-6826(98)00072-8.
- Gao, H., J. Xu, and Q. Wu, 2010: Seasonal and QBO variations in the OH nightglow emission observed by TIMED/SABER. *J. Geophys. Res.*, **115**, A06313, doi:10.1029/2009JA014641.
- Heppner, J. P., and L. H. Meredith, 1958: Nightglow emission altitudes from rocket measurements. *J. Geophys. Res.*, **63**, 51–65, doi:10.1029/JZ063i001p00051.

- Hines, C. O., 1960: Internal gravity waves at ionospheric heights. *Can. J. Phys.*, **38**, 1441–1481, doi:10.1139/p60-150.
- Kaufmann, M., C. Lehmann, L. Hoffmann, B. Funke, M. López-Puertas, C. von Savigny, and M. Riese, 2008: Chemical heating rates derived from SCIAMACHY vibrationally excited OH limb emission spectra. *Adv. Space Res.*, **41**, 1914–1920, doi:10.1016/j.asr.2007.07.045.
- Keckhut, P., and Coauthors, 2010: Mid-latitude ozone monitoring with the GOMOS-ENVISAT experiment version 5: The noise issue. *Atmos. Chem. Phys.*, **10**, 11 839–11 849, doi:10.5194/acp-10-11839-2010.
- McLennan, J. C., and J. H. McLeod, 1927: On the wave-length of the green auroral line in the oxygen spectrum. *Proc. Roy. Soc. London*, **115A**, 515–527.
- Meinel, A. B., 1950: OH emission bands in the spectrum of the night sky. I. *Astrophys. J.*, **111**, 555, doi:10.1086/145296.
- Melo, S. M. L., R. P. Lowe, and J. P. Russel, 2000: Double-peaked hydroxyl airglow profiles observed from WINDII/UARS. *J. Geophys. Res.*, **105**, 12 397–12 403, doi:10.1029/1999JD901169.
- Meriwether, J. W., Jr., 1989: A review of the photochemistry of selected nightglow emissions from the mesopause. *J. Geophys. Res.*, **94**, 14 629–14 646, doi:10.1029/JD094iD12p14629.
- Mlynczak, M. G., 1997: Energetics of the mesosphere and lower thermosphere and the SABER experiment. *Adv. Space Res.*, **20**, 1177–1183, doi:10.1016/S0273-1177(97)00769-2.
- Pérot, K., A. Hauchecorne, F. Montmessin, J.-L. Bertaux, L. Blanot, F. Dalaudier, D. Fussen, and E. Kyrölä, 2010: First climatology of polar mesospheric clouds from GOMOS/ENVISAT stellar occultation instrument. *Atmos. Chem. Phys.*, **10**, 2723–2735, doi:10.5194/acp-10-2723-2010.
- Russell, M. J., III, M. G. Mlynczak, L. L. Gordley, J. J. Tansock, and R. W. Esplin, 1999: Overview of the SABER experiment and preliminary calibration results. *Optical Spectroscopic Techniques and Instrumentation for Atmospheric and Space Research III*, A. M. Larar, Ed., International Society for Optical Engineering (SPIE Proceedings, Vol. 3756), 277, doi:10.1117/12.366382.
- Shepherd, G. G., C. D. Anger, L. H. Brace, J. R. Burrows, W. J. Heikkila, J. Hoffman, E. J. Maier, and J. H. Whitteker, 1973: An observation of polar aurora and airglow from the ISIS-II spacecraft. *Planet. Space Sci.*, **21**, 819–829, doi:10.1016/0032-0633(73)90099-8.
- Slipher, V. M., 1929: Emissions in the spectrum of the light of the night sky. *Publ. Astron. Soc. Pac.*, **41**, 262–264.
- Sofieva, V., J. Tamminen, H. Haario, E. Kyrölä, and M. Lehtinen, 2004: Ozone profile smoothness as a priori information in the inversion of limb measurements. *Ann. Geophys.*, **22**, 3411–3420, doi:10.5194/angeo-22-3411-2004.
- Solomon, S., R. W. Portmann, R. W. Sanders, J. S. Daniel, W. Madsen, B. Bartram, and E. G. Dutton, 1999: On the role of nitrogen dioxide in the absorption of solar radiation. *J. Geophys. Res.*, **104**, 12 047–12 058, doi:10.1029/1999JD900035.
- Suzuki, H., Y. Tomikawa, M. Taguchi, T. Nakamura, and M. Tsutsumi, 2010: Variations of OH rotational temperature over Syowa Station in the austral winter of 2008. *Earth Planets Space*, **62**, 655–661, doi:10.5047/eps.2010.07.010.
- Torr, M. R., P. B. Hays, B. C. Kennedy, and J. C. G. Walker, 1977: Intercalibration of airglow observatories with the Atmosphere Explorer satellite. *Planet. Space Sci.*, **25**, 173–184, doi:10.1016/0032-0633(77)90022-8.
- Yee, J.-H., G. Crowley, R. G. Roble, W. R. Skinner, M. D. Burrage, and P. B. Hays, 1997: Global simulations and observations of O(<sup>1</sup>S), O<sub>2</sub>(<sup>1</sup>Σ) and OH mesospheric nightglow emissions. *J. Geophys. Res.*, **102**, 19 949–19 968, doi:10.1029/96JA01833.